J. Fluid Mech. (2012), *vol.* 700, *pp.* 5–15. © Cambridge University Press 2012
doi:10.1017/jfm.2012.5

Dissipation, enstrophy and pressure statistics in turbulence simulations at high Reynolds numbers

P. K. Yeung[1]†, D. A. Donzis[2] and K. R. Sreenivasan[3]

[1] Schools of Aerospace Engineering, Computational Science and Engineering, and Mechanical Engineering, Georgia Institute of Technology, Atlanta, GA 30332, USA

[2] Department of Aerospace Engineering, Texas A&M University, College Station, TX 77843, USA

[3] Courant Institute of Mathematical Sciences and Physics Department, New York University, New York, NY 10012, USA

(Received 31 October 2011; revised 30 December 2011; accepted 31 December 2011; first published online 8 February 2012)

We use data from well-resolved direct numerical simulations at Taylor-scale Reynolds numbers from 140 to 1000 to study the statistics of energy dissipation rate and enstrophy density (i.e. the square of local vorticity). Despite substantial variability in each of these variables, their extreme events not only scale in a similar manner but also progressively tend to occur spatially together as the Reynolds number increases. Though they possess non-Gaussian tails of enormous amplitudes, ratios of some characteristic properties can be closely linked to those of isotropic Gaussian random fields. We present results also on statistics of the pressure Laplacian and conditional mean pressure given both dissipation and enstrophy. At low Reynolds number intense negative pressure fluctuations are preferentially associated with rotation-dominated regions but at high Reynolds number both high dissipation and high enstrophy have similar effects.

Key words: homogeneous turbulence, intermittency, turbulence simulation

1. Introduction

Fluctuations in the energy dissipation rate and the enstrophy density (with the words 'rate' and 'density' omitted hereafter for brevity, as in common usage), defined by

$$\epsilon = 2\nu s_{ij} s_{ij}; \quad \Omega = \omega_i \omega_i, \tag{1.1}$$

respectively, are two different descriptors of the structure of small-scale turbulence (Sreenivasan & Antonia 1997). Here, ν is the viscosity, s_{ij} is the strain rate, ω_i is the vorticity and the summation rule applies to repeated tensor subscripts. The effects of extreme dissipation and enstrophy are quite distinct: for example, extreme dissipation represents intense local straining which can break flame surfaces in turbulent combustion, while large enstrophy represents strong vortical motions which can lead to preferential concentration of inertial particles in multiphase flows.

† Email address for correspondence: pk.yeung@ae.gatech.edu

Although in homogeneous turbulence these quantities have the same mean value (if Ω is multiplied by ν), a common finding at moderate Reynolds numbers is that enstrophy is more intermittent than dissipation (Kerr 1985; Chen, Sreenivasan & Nelkin 1997). However, data from recent direct numerical simulations (DNS) at high resolution (Donzis, Yeung & Sreenivasan 2008) focused on extreme events in dissipation and enstrophy support theoretical arguments (Nelkin 1999) that these two quantities scale similarly at high Reynolds numbers. This is the first facet we explore in this paper.

Even if ϵ and Ω scale similarly as each other, it is the differences in their instantaneous spatial distributions (i.e. the mismatch of spatial regions where one of them is high or low with those where the other is high or low) that defines the Laplacian of pressure which, in isotropic turbulence, satisfies

$$\nabla^2(p/\rho) = (\Omega - \epsilon/\nu)/2. \tag{1.2}$$

Although the pressure fluctuation at a point is not prescribed entirely by local values of $Q \equiv \nabla^2(p/\rho)$, this Poisson equation justifies using it as a rough diagnostic for small-scale vortical structures (Jeong & Hussain 1995). The properties of ϵ, Ω and p were explored numerically earlier by Pumir (1994) at a low Reynolds number. However, the Reynolds number dependence of the pressure Laplacian is not understood, and the intermittency in ϵ and Ω is likely to lead to qualitative differences between results at 'low' and 'high' Reynolds numbers. Investigation of this aspect is our second task here.

We use results from DNS of forced isotropic turbulence, at grid resolution up to 4096^3, to characterize the dissipation and enstrophy fluctuations simultaneously, and to explore their relationship to pressure. In § 2 we give an overview of the numerical simulations, which are the best resolved available at the Reynolds numbers of our database. Results on dissipation and enstrophy, and the connection to pressure fluctuations, are presented in §§ 3 and 4, respectively. Brief concluding remarks are provided in § 5.

2. Simulation approach and database

As in Donzis *et al.* (2008), our results are obtained from Fourier pseudo-spectral calculations with second-order Runge–Kutta integration in time. The turbulence is forced numerically at the large scales, using a scheme first used in Donzis & Yeung (2010). Increased resolution made possible by advances in high-performing computing has been used both to increase the Reynolds number and to resolve small scales better (Yakhot & Sreenivasan 2005; Donzis *et al.* 2008). The condition for the latter is expressed by the dimensionless parameter $k_{max}\eta$, where $k_{max} = \sqrt{2}N/3$ is the highest wavenumber resolved on an N^3 grid and η is the Kolmogorov scale. (The ratio of grid spacing Δx to η is roughly $3/k_{max}\eta$.) Typically, in simulations aimed at increasing the Reynolds number (see Ishihara, Gotoh & Kaneda (2009)), $k_{max}\eta$ is around 1.4–1.5, which corresponds to $\Delta x/\eta \approx 2$. In this work, since resolution is important, we have used higher values of $k_{max}\eta$ (i.e. finer grids) for all targeted Reynolds numbers except the highest. Although on occasion we compare results obtained with different degrees of resolution at different Reynolds numbers, the interpretation of the data takes account of possible differences in this regard.

Table 1 lists the basic parameters, from the best-resolved simulations at five Reynolds numbers ($140 \leqslant R_\lambda \leqslant 1000$, rounded to the nearest 10). Here $R_\lambda \equiv u'\lambda/\nu$, where u' is the root-mean-square (r.m.s.) velocity and λ is the Taylor microscale.

R_λ	140	240	380	600	1000
$k_{max}\eta$	11.2	11.2	2.7	2.7	1.3
N	2048	4096	2048	4096	4096
$T/(L_1/u')$	1.96	2.87	4.61	3.36	3.59
N_R	35	20	48	33	20
$\langle\epsilon\rangle L_1/u'^3$	0.458	0.449	0.451	0.470	0.464
μ_3 of $\nabla_\parallel u$	-0.52 ± 0.01	-0.56 ± 0.06	-0.59 ± 0.00	-0.62 ± 0.00	-0.63 ± 0.00
μ_4 of $\nabla_\parallel u$	5.68 ± 0.06	6.82 ± 0.11	8.06 ± 0.11	10.01 ± 0.32	11.17 ± 0.31
$\{\langle\Omega'^2\rangle/\langle\epsilon'^2\rangle\}$	1.83 ± 0.02	1.89 ± 0.03	1.93 ± 0.02	1.95 ± 0.04	1.98 ± 0.02
$\{\langle\Omega'^3\rangle/\langle\epsilon'^3\rangle\}$	4.58 ± 0.24	5.05 ± 0.48	4.30 ± 1.26	3.28 ± 1.42	2.86 ± 0.93
$\{\langle\Omega'^4\rangle/\langle\epsilon'^4\rangle\}$	13.5 ± 2.8	15.6 ± 5.7	9.4 ± 7.1	5.6 ± 5.9	3.3 ± 1.3

TABLE 1. Selected DNS parameters at five different Reynolds numbers: number of grid points in each direction, spatial resolution parameter, period for time averaging, number of snapshots analysed, normalized mean dissipation rate, skewness and flatness of longitudinal velocity gradients, and the ratios between moments of normalized dissipation ($\epsilon' = \epsilon/\langle\epsilon\rangle$) and enstrophy ($\Omega' = \Omega/\langle\Omega\rangle$). Angled brackets denote averaging in space and over multiple snapshots when applicable, while curly braces represent ensemble averaging of the ratios of spatially averaged moments instead of the moments themselves. We include 95 % confidence intervals based on Student's t distribution in statistical theory. In all cases the box length L_0 is 2π, $L_1/L_0 \sim 0.2$ and R_λ is increased by reducing viscosity and keeping forcing parameters unchanged.

We have included the simulation time period T measured in large-eddy time scales (L_1/u', where L_1 is longitudinal integral length scale) and the number of instantaneous snapshots (N_R) analysed. Clearly, a long simulation is desirable for sampling accuracy but finite resources have limited the value of T attainable at higher Reynolds numbers. However, since intense fluctuations of intermittent variables (such as ϵ and Ω) are relatively short lived, a large N_R is still helpful even if snapshots used for ensemble averaging are not far apart in integral time. As R_λ increases, the mean dissipation rate scales with u'^3/L_1 (Sreenivasan 1998) following classical arguments. The longitudinal velocity gradient $\nabla_\parallel u$ is negatively skewed, and becomes increasingly non-Gaussian as R_λ increases. Both ϵ and Ω are normalized by their mean values. Typically, in simulations with modest resolution, high-order moments of dissipation and enstrophy (both of which increase with Reynolds number) are underestimated but the ratios between moments of the two are nearly unaffected (Donzis *et al.* 2008).

Because rare events of high intensity play a strong role, statistical convergence in the high-order moments of ϵ and Ω is difficult to achieve. Figure 1 shows that the fourth moments can vary between different snapshots from the same simulation by as much as four orders of magnitude. Improved resolution compounds the difficulty as more extreme events are captured. In part (*a*) of this figure all data symbols lie above the diagonal line, with data at larger values (mostly from simulations at higher R_λ) generally closer to the diagonal, while in part (*b*) the ratio of the two fourth moments (last row of table 1) appears to approach unity in the high-R_λ limit. In part (*a*) there is seemingly a change in behaviour at normalized moments around $O(10^5)$ between two groups of data points. This feature may bear some relation to the mixing transition proposed by Dimotakis (2000) and interpreted by Yakhot (2008) as a consequence of strong fluctuations in the dissipation length scale.

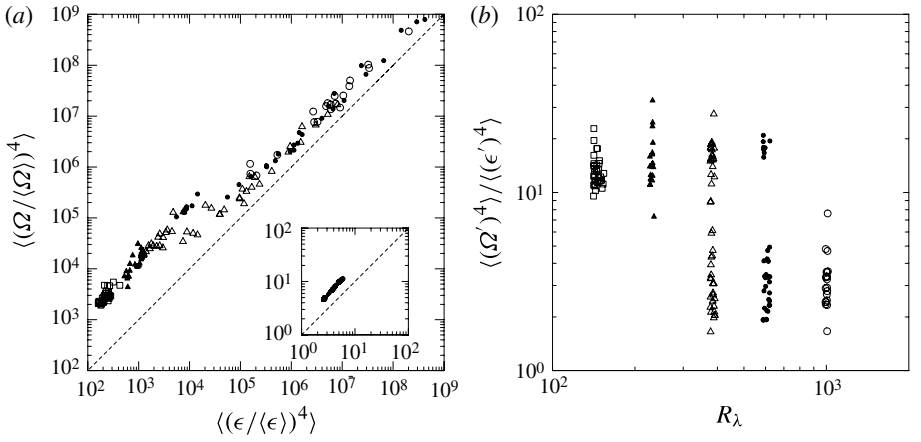

FIGURE 1. Data on spatially averaged moments of normalized dissipation and enstrophy for each snapshot, with different symbols for the five simulations listed in table 1 (□, ▲, △, • and ○, respectively). In (*a*) the moments are plotted against each other (inset shows second moments). In (*b*) the ratio of fourth moments is plotted against the Reynolds number in each snapshot.

3. Fluctuations of dissipation and enstrophy

The scaling of extreme events in ϵ or Ω is closely related to the behaviour of the wide tails of their probability density functions (p.d.f.s). Recent DNS data (Donzis *et al.* 2008) have suggested that the tails of p.d.f.s of ϵ and Ω approach each other for $R_\lambda \approx 400$ onwards, in the range of fluctuations beyond some 1500 times the mean. Figure 2 shows the contrast between results for $R_\lambda \approx 240$ and $R_\lambda \approx 1000$: 'moderately large' values of Ω' (say, $O(100)$ times the mean) are more likely than ϵ' of comparable magnitude, while extreme values of both occur with about equal probability. In general, large values of ϵ and Ω contribute more to the moments $\langle\epsilon'^p\rangle$ and $\langle\Omega'^p\rangle$ as the order of the moment (i.e. p) increases. Consequently from figure 2 we expect that the ratio $\langle\Omega'^p\rangle/\langle\epsilon'^p\rangle$ will increase with R_λ beyond some R_λ if p is low enough, but decrease if p is sufficiently large. Indeed, in the last three rows of table 1 we observe a decrease with R_λ for $p = 4$ in contrast to a slight increase for $p = 2$.

To investigate if intense fluctuations of ϵ and Ω occur simultaneously in space and time, we consider the joint p.d.f. of $\epsilon/\langle\epsilon\rangle$ and $\Omega/\langle\Omega\rangle$. Figure 3 shows contours of this joint p.d.f. at $R_\lambda \approx 240$ and 1000. The first quadrant represents high dissipation and high enstrophy while the third quadrant represents low values of both. Strain-dominated regions, if defined by the criterion $\epsilon > \nu\Omega$, occupy the lower triangular half, below the diagonal dashed line of slope unity through the origin. Since both $\epsilon/\langle\epsilon\rangle$ and $\Omega/\langle\Omega\rangle$ are plotted on logarithmic scales and contour levels are also spaced logarithmically, approximate linear spacing of contour lines in the first quadrant reflects nearly exponential (or mildly stretched exponential) behaviour. If dissipation and enstrophy scale alike, one could expect a trend towards symmetry across the diagonal noted above, and the contour patterns in the second quadrant ($\epsilon < \langle\epsilon\rangle$ and $\Omega > \langle\Omega\rangle$) and fourth quadrant ($\epsilon > \langle\epsilon\rangle$ and $\Omega < \langle\Omega\rangle$) would resemble each other strongly. At higher Reynolds number, these symmetries become increasingly evident in the first quadrant, although differences remain in the third. Furthermore, at higher R_λ a narrow protuberance pointing in the direction of increasing ϵ and Ω is seen to develop along the diagonal line. The apparent convergence of this protuberance

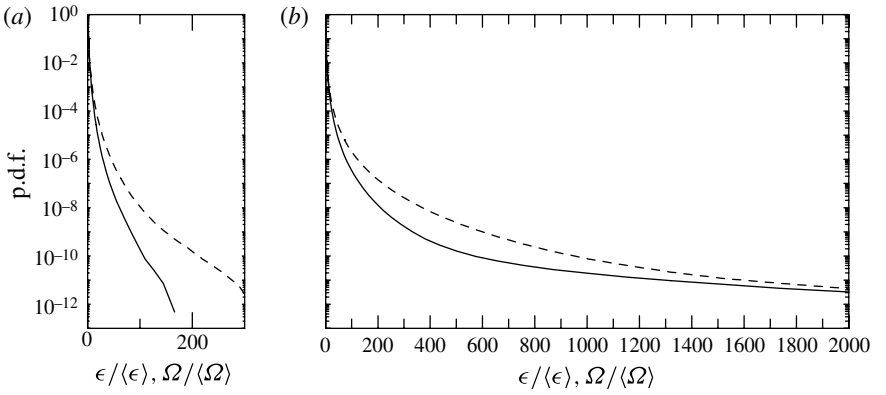

FIGURE 2. p.d.f.s of normalized dissipation (solid lines) and enstrophy density (dashed lines) from two 4096^3 simulations. (*a*) $R_\lambda \approx 240$, $k_{max}\eta \approx 11$; (*b*) $R_\lambda \approx 1000$, $k_{max}\eta \approx 1.4$.

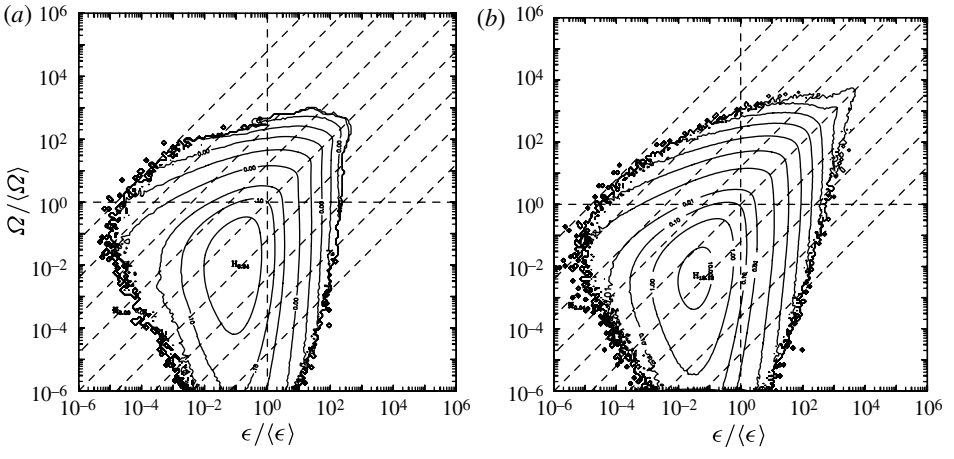

FIGURE 3. Contour plots of the joint p.d.f.s of normalized dissipation and enstrophy density, at (*a*) $R_\lambda \approx 240$ and (*b*) $R_\lambda \approx 1000$. Contour levels are 10, 1, 0.1 and 0.01, and decreasing by factors of 100 in successive lines beyond. Dashed lines of slope 1 are added to help compare strain-dominated and rotation-dominated regions.

onto the diagonal line provides strong evidence that extreme events in dissipation and enstrophy tend to occur together at higher Reynolds numbers. The single-point joint p.d.f., however, does not provide information on the spatial extent in which such correlations are maintained between regions of high ϵ and high Ω.

To assess the relative likelihood of strain-dominated and rotation-dominated regions, we can consider the probabilities of the events $\{\epsilon' > \Omega'\}$ and $\{\Omega' > \epsilon'\}$ – or, more generally, the p.d.f. of the dissipation–enstrophy ratio, $\gamma = \epsilon/(\nu\Omega)$. Since both ϵ and Ω can take very small values (close to zero), γ can span a very wide range. Figure 4 shows that this p.d.f. is highly non-symmetric, with peak values occurring in the range $0.1 \leqslant \gamma \leqslant 1$ but also a wide tail on the right, extending to at least $\gamma \sim 10^7$. Since the largest samples of ϵ' and Ω' are at most $O(10^4)$ even in the $R_\lambda \approx 1000$ simulation, both the smallest and the largest values of γ are the result of very small instead of very large values of ϵ' or Ω'. The p.d.f.s at $R_\lambda \approx 240$ and 1000 are extremely

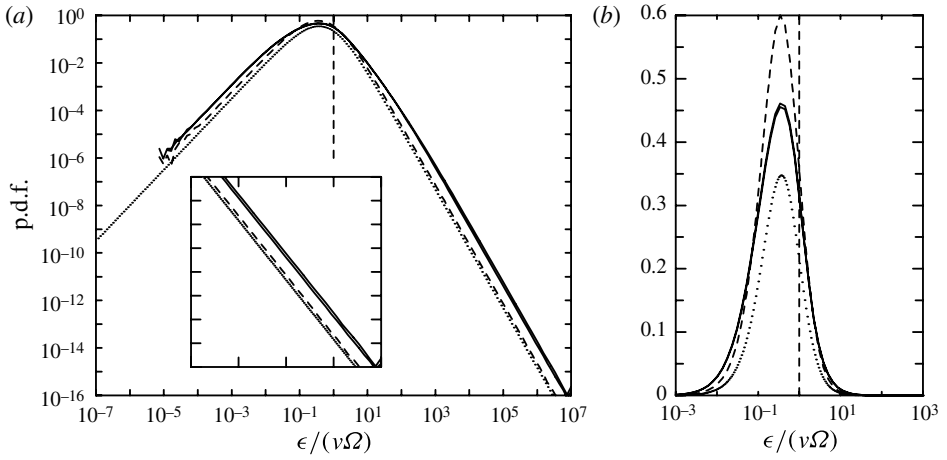

FIGURE 4. p.d.f. of the ratio $\gamma = \epsilon/(\nu\Omega)$, in (*a*) log–log and (*b*) log–linear scales. DNS data at $R_\lambda \approx 240$ and 1000 are drawn as two solid lines which almost coincide. Dashed lines represent a Gaussian random field with the same energy spectrum as DNS at $R_\lambda \approx 1000$. Dotted lines represent an F distribution estimate (discussed in the text). The inset in (*a*) shows a zoom-in for γ in the range 10^3 to 10^7, while (*b*) shows γ in the range 10^{-3} to 10^3, using log–linear scales.

close, both on log–log scales, which emphasize extreme values of the variables (with power-law behaviour evident in part *a*), and log–linear scales, which emphasize the more moderate magnitudes.

The apparent closeness between the p.d.f.s of γ at $R_\lambda \approx 240$ and $R_\lambda \approx 1000$ suggests the observed behaviour is in part kinematic – which should then be present also in isotropic Gaussian random fields (GRFs) constructed to have the same energy spectrum as the DNS data but without Navier–Stokes dynamics. For a GRF all components of velocity gradient are normally distributed and independent, except for the incompressibility condition that relates the longitudinal gradients. This means that Ω is the sum of squares of all three Gaussians and hence behaves as chi-square of order three, while ϵ, by incompressibility, is close to chi-square of order five. It follows that, for a GRF, γ would follow closely the so-called F distribution. In particular, if χ_n^2 and χ_m^2 are chi-squared variables of orders n and m, then the variable $x = (\chi_n^2/n)/(\chi_m^2/m)$ has the p.d.f.

$$f_{n,m}(x) = \frac{\Gamma\left(\frac{1}{2}(m+n)\right) n^{n/2} m^{m/2}}{\Gamma(n/2)\Gamma(m/2)} \frac{x^{n/2-1}}{(m+nx)^{(m+n)/2}}, \tag{3.1}$$

where $\Gamma(\cdot)$ is the Gamma function. In figure 4 this expression, with $n = 5$ and $m = 3$, is found to be close to the GRF result, especially when γ is large. Furthermore, according to (3.1), the p.d.f. of the F distribution varies as $x^{n/2-1}$ for $x \to 0$ and as $x^{-(1+m/2)}$ for $x \to \infty$, which in our application would lead to power laws of slopes close to 1.5 and -2.5 for $\gamma \to 0$ and $\gamma \to \infty$, respectively. Even the DNS data (with non-Gaussian features) show similar power laws. This result can be understood by noting that the tails of the p.d.f. of γ are dominated by very small values of ϵ and Ω, which in turn imply very small velocity gradients. In other words, these power-law tails are produced by samples close to the core of the velocity gradient p.d.f.s in a

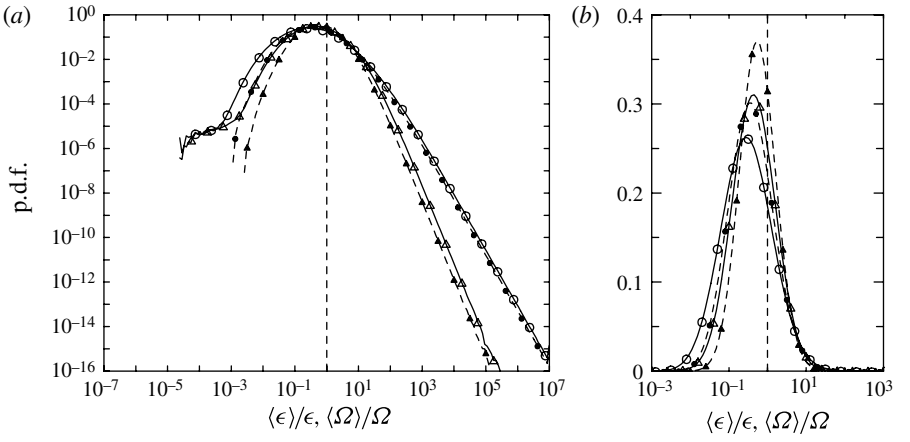

FIGURE 5. p.d.f.s of reciprocals of normalized dissipation and enstrophy in (*a*) log–log and (*b*) log–linear scales. Solid lines are for $R_\lambda \approx 1000$ ($\triangle$ for $\langle\epsilon\rangle/\epsilon$, $\circ$ for $\langle\Omega\rangle/\Omega$). Dashed lines are for $R_\lambda \approx 240$ ($\blacktriangle$ for $\langle\epsilon\rangle/\epsilon$, $\bullet$ for $\langle\Omega\rangle/\Omega$).

regime where non-Gaussian effects are small. In contrast, intense ϵ' and Ω' (often within one order of magnitude of each other) are confined near the core of the p.d.f. of γ, where (as seen in part *b* of figure 4) both GRF and F-distribution results differ substantially from DNS. We also note in passing that the results discussed here cannot be explained by invoking log-normality for $\ln\epsilon$ and $\ln\Omega$ independently: it is known that $\ln\epsilon$ and $\ln\Omega$ have a positive correlation coefficient of order 0.5 which increases weakly with R_λ (Yeung & Pope 1989), and $\ln\gamma$ departs from Gaussian more than $\ln\epsilon$ or $\ln\Omega$.

Since the tails in figure 4 are dominated by extremely small ϵ and Ω, it is useful to examine the p.d.f.s of the reciprocals of the dissipation and enstrophy, in the form $\langle\epsilon\rangle/\epsilon$ and, similarly, $\langle\Omega\rangle/\Omega$. (These p.d.f.s are directly related to those of $\epsilon/\langle\epsilon\rangle$ and $\Omega/\langle\Omega\rangle$ but show the behaviour of small values more clearly.) In part (*a*) of figure 5 the p.d.f.s of $\langle\epsilon\rangle/\epsilon$ and $\langle\Omega\rangle/\Omega$ at $R_\lambda \approx 1000$ are seen to converge on the left, corresponding to the far tails in figure 2. To the right of the figure, extremely small Ω are clearly much more probable than extremely small ϵ; this trend is consistent with the phenomenological picture (e.g. Jimenez *et al.* 1993) that large enstrophy is isolated and surrounded by large regions of low vorticity. The p.d.f. of $\langle\Omega\rangle/\Omega$ also shows a power-law tail of slope -2.5 for large values of the ratio, which is consistent with very small Ω being close to chi-square distributed regardless of Reynolds number. Other ranges of the variable show significant Reynolds number dependence, which is clearer in part (*b*) of the figure: e.g. as R_λ increases the probability for ϵ' and Ω' to occur in the range 1–100 is reduced.

4. Relation to the pressure field

As noted earlier, (1.2) shows that pressure fluctuations are associated loosely with the joint state of dissipation and enstrophy via the pressure Laplacian, denoted by $Q \equiv \nabla^2(p/\rho)$. Since enstrophy fluctuations of intermediate magnitudes are more likely than dissipation fluctuations of similar magnitude, one can expect the probability distribution of Q to be positively skewed. Further, if intense dissipation and intense enstrophy tend to occur together, the distribution of Q should be narrower than those

R_λ	140	240	380	600	1000
N	2048	4096	2048	4096	4096
$\langle(\epsilon')^2\rangle$	2.65 ± 0.02	3.19 ± 0.05	3.78 ± 0.05	4.65 ± 0.08	5.21 ± 0.12
$\langle(\Omega')^2\rangle$	4.85 ± 0.05	6.05 ± 0.12	7.31 ± 0.12	9.12 ± 0.12	10.31 ± 0.20
$\langle(Q')^2\rangle$	0.74 ± 0.01	0.93 ± 0.02	1.13 ± 0.02	1.40 ± 0.02	1.57 ± 0.03
$\langle(\epsilon')^3\rangle$	17 ± 0.4	31 ± 1.5	166 ± 70	2214 ± 1510	1258 ± 710
$\langle(\Omega')^3\rangle$	77 ± 3	158 ± 12	473 ± 120	4517 ± 2900	2800 ± 1266
$\langle(Q')^3\rangle$	4.3 ± 0.2	9.4 ± 0.8	17 ± 1	40 ± 8	38 ± 3
$\{\langle(Q')^2\rangle/\langle(\epsilon')^2\rangle\}$	0.28 ± 0.00	0.29 ± 0.01	0.30 ± 0.01	0.30 ± 0.01	0.30 ± 0.01
$\{\langle(Q')^3\rangle/\langle(\epsilon')^3\rangle\}$	0.26 ± 0.02	0.30 ± 0.04	0.26 ± 0.01	0.15 ± 0.00	0.07 ± 0.07
$\{\langle(Q')^4\rangle/\langle(\epsilon')^4\rangle\}$	0.45 ± 0.01	0.55 ± 0.26	0.28 ± 0.29	0.10 ± 0.01	0.01 ± 0.01

TABLE 2. Comparison of moments of normalized pressure Laplacian $Q' \equiv \nabla^2(p/\rho)/(\langle\epsilon\rangle/\nu)$ with those of $\epsilon' = \epsilon/\langle\epsilon\rangle$ and $\Omega' = \Omega/\langle\Omega\rangle$, from the same datasets as in table 1. Fourth moments of ϵ' and Ω' are omitted here because of their great statistical variability, especially at higher R_λ.

R_λ	C_1	C_2	C_3	C_4	C_5	C_6
140	-0.31 ± 0.005	0.23 ± 0.01	-0.18 ± 0.02	0.16 ± 0.02	-0.15 ± 0.02	0.14 ± 0.03
1000	-0.049 ± 0.002	0.037 ± 0.003	-0.037 ± 0.01	0.14 ± 0.07	-0.29 ± 0.1	0.40 ± 0.1

TABLE 3. Correlation coefficients between nth power of p and $\nabla^2(p/\rho)$, for $n = 1$ to 6, with 90 % confidence intervals.

of ϵ and Ω, the contrast being greater at higher Reynolds number. In table 2 we present data on normalized moments to support this expectation. In particular, as the Reynolds number increases, while all normalized moments grow, high-order moments of Q grow more weakly than those of ϵ and Ω. At the highest R_λ shown, the normalized third-order moments of Q are nearly two orders of magnitude smaller than those of ϵ and Ω, and even more so at fourth order. The behaviour of the mean square of the normalized Laplacian can also be related to the correlation coefficient between dissipation and enstrophy, which is about 0.5 at $R_\lambda \approx 140$ and 0.73 at $R_\lambda \approx 1000$. The ensemble-averaged ratio between normalized moments of Q and those of ϵ and Ω also shows a decrease for higher-order moments at sufficiently high R_λ.

To connect the observations above to the pressure fluctuation itself, we consider the nature of solutions to (1.2). For an unbounded flow domain (and periodic domain in the DNS) a formal solution is $p/\rho = -1/4\pi \int Q(\boldsymbol{x}')/|\boldsymbol{x} - \boldsymbol{x}'|\, \mathrm{d}^3\boldsymbol{x}'$, which implies that a sufficiently large positive Q (with $\Omega > \epsilon/\nu$) at or close to a given point in space can lead to strongly negative pressure fluctuations. In addition, the result $\langle p\nabla^2(p/\rho)\rangle = -\langle\nabla(p/\rho)\cdot\nabla(p/\rho)\rangle$ (due to homogeneity) implies that p and Q must be negatively correlated. To quantify the correlation between increasingly intense events in p and Q, we compute the correlation coefficients, say C_n, between p^n and Q^n. If intense events in ϵ and/or Ω (resulting in large Q) are closely related, the magnitude of C_n should increase with n. Results in table 3 for $n = 1$ to 6 show that this expectation holds well at $R_\lambda \approx 1000$ (whereas, in contrast, the level of correlation at $R_\lambda \approx 140$ decreases with n). Furthermore, the increase in correlation level at $R_\lambda \approx 1000$ is stronger for even moments (which are insensitive to the sign of actual samples of Q) than for odd moments. This suggests a significant association also exists

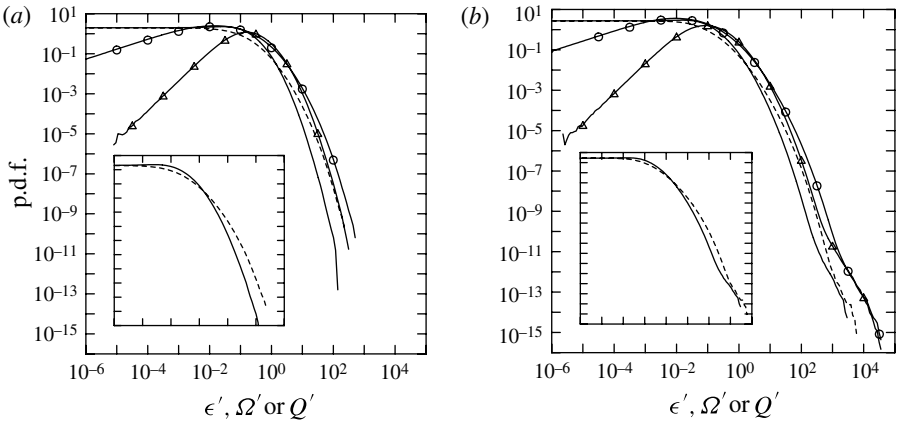

FIGURE 6. p.d.f.s of normalized ϵ, Ω and $Q \equiv \nabla^2(p/\rho)$ from simulations at (*a*) $R_\lambda \approx 240$ and (*b*) $R_\lambda \approx 1000$. Lines with triangles and circles represent $\epsilon/\langle\epsilon\rangle$ and $\Omega/\langle\Omega\rangle$, respectively. Unmarked dashed lines and solid lines represent $Q' = Q/(\langle\epsilon\rangle/\nu) > 0$ and $Q' < 0$ (plotted in absolute value), respectively. Insets give a clearer comparison between results for $Q' > 0$ and $Q' < 0$.

between strongly negative p and strongly negative Q, which correspond to regions of the flow dominated by intense strain rate.

In figure 6 we compare the p.d.f. of the normalized pressure Laplacian with those of dissipation and enstrophy. To retain the use of logarithmic scales (which allow closer observation of the tails of the distribution), we have plotted the p.d.f. of Q in the ranges of $Q > 0$ and $Q < 0$ as separate lines. Overall, the probability of events of $Q < 0$ (i.e. $\epsilon > \nu\Omega$) is around 60–65 %, with very little dependence on R_λ. Since the p.d.f. of Q is smooth at $Q = 0$, as $|Q| \to 0$, it tends to the same limiting plateau for both $Q > 0$ and $Q < 0$. Because large Ω is more likely than large ϵ, large positive values of Q are more likely than negative values of the same magnitude. The tails of the p.d.f. of Q are clearly not as wide as those for ϵ and Ω. However, in the case of $R_\lambda \approx 1000$, at extreme values of $|Q|$, the p.d.f.s for Q of different signs become close again. Since $Q > 0$ when $\Omega > \epsilon/\nu$ and $Q < 0$ when $\Omega < \epsilon/\nu$, these observations are consistent with suggestions that the most intense values of ϵ and Ω tend to occur together at the higher Reynolds number.

To relate the joint state of ϵ and Ω to the pressure field, we have also computed the conditional mean pressures given ϵ and Ω simultaneously, i.e. $\langle p|\epsilon, \Omega\rangle$, as shown in figure 7. This doubly-conditioned quantity is largely confined to the same envelopes defined by the joint p.d.f. contours shown earlier, but with a greater degree of sampling noise at the edges. At both Reynolds numbers, positive contour levels (solid lines) reside primarily in the third quadrant ($\epsilon < \langle\epsilon\rangle$ and $\Omega < \langle\Omega\rangle$) while negative values dominate elsewhere. At low R_λ negative values of $\langle p|\epsilon, \Omega\rangle$ are preferentially associated with large values of Ω, which implies rotation-dominated regions have a stronger tendency than strain-dominated regions to produce a negative mean pressure when averaged over the conditional samples. However, as the Reynolds number increases, the most intensely negative contour values are increasingly found near the diagonal line, precisely at locations where intense events occur simultaneously in both dissipation and enstrophy.

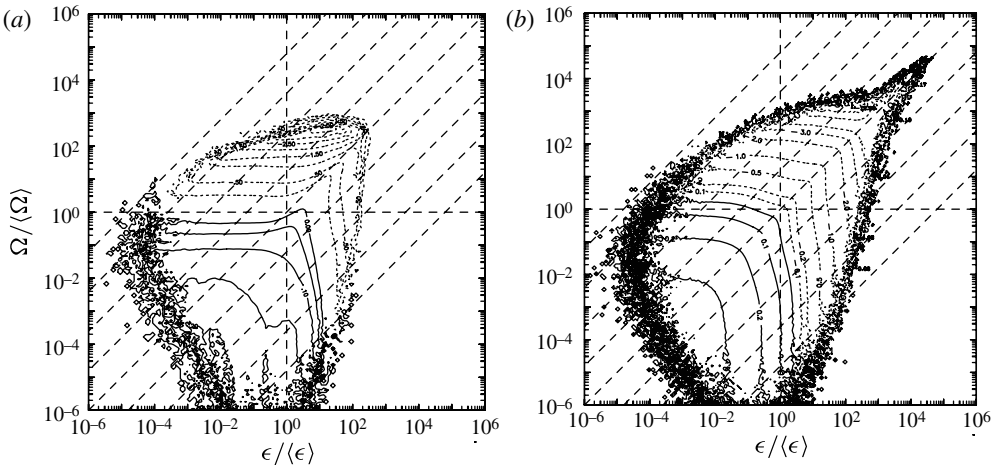

FIGURE 7. Contour plots of conditional mean pressure (normalized by its root-mean-square fluctuation) given normalized ϵ and Ω, at (*a*) $R_\lambda \approx 240$ and (*b*) $R_\lambda \approx 1000$. Contour levels used are: -3.5, -3, -2.5, -2, -1.5, -1, -0.5, -0.25, 0, 0.05, 0.1, 0.15 and 0.2. Solid and dashed curves denote positive and negative contour levels, respectively.

5. Conclusions

DNS data for isotropic turbulence at high resolution and Taylor-scale Reynolds numbers from 140 to 1000 are used to study the statistical behaviour of fluctuations of dissipation rate, enstrophy density and the Laplacian of pressure. We focus on two questions: (a) as the Reynolds number increases, do dissipation and enstrophy scale in the same way, and what does it imply for their coincidence (or otherwise) in physical space? (b) What can we learn about pressure fluctuations if we know the statistics of ϵ and Ω?

With regard to (a), despite significant statistical variability, moments at various orders and joint p.d.f.s indicate that, at sufficiently high Reynolds number (only recently achievable in DNS) extreme events in dissipation and enstrophy not only scale in a similar manner but also progressively tend to occur together at high Reynolds numbers. Events of dissipation exceeding enstrophy occur with a probability slightly higher than 60 %, while extreme values of the ratio $\epsilon/(\nu\Omega)$ are dominated by occurrences of very small dissipation and enstrophy associated with the near-Gaussian cores of velocity gradient p.d.f.s. With regard to (b), we find that the Laplacian of pressure has a positively skewed p.d.f. with narrower tails compared with dissipation and enstrophy. As the Reynolds number increases these tails become more nearly symmetric, while both high dissipation and high enstrophy become substantially associated with negative pressure fluctuations.

The present study provides clear evidence that turbulence simulations at high Reynolds number with sufficient resolution are now capable of facilitating new insights that previous simulations could not provide. An important underlying question is what is the minimum Reynolds number needed to observe asymptotic behaviour in the statistics of small-scale turbulence, which likely will depend on the class of quantity examined. Results on longitudinal and transverse structure functions, and on the statistics of local averages as a function of averaging scale, will be reported separately.

Acknowledgements

We gratefully knowledge support from the National Science Foundation (NSF), via collaborative grants CBET-0553867 and 1139037 (PKY) and 0553602 (KRS). We used advanced computational resources at the Texas Advanced Computing Center (at University of Texas at Austin), National Institute for Computational Sciences (at the University of Tennessee) and National Center for Computational Sciences (at Oak Ridge National Laboratory). We thank the anonymous reviewers and Professors T. Gotoh, M. Nelkin, A. Pumir and B. L. Sawford for helpful comments. K. Iyer and D. Buaria helped retrieve some of the datasets from mass storage systems.

REFERENCES

CHEN, S., SREENIVASAN, K. R. & NELKIN, M. 1997 Inertial range scalings of dissipation and enstrophy in isotropic turbulence. *Phys. Rev. Lett.* **79**, 1253–1256.

DIMOTAKIS, P. 2000 The mixing transition in turbulent flows. *J. Fluid Mech.* **409**, 69–97.

DONZIS, D. A. & YEUNG, P. K. 2010 Resolution effects and scaling in numerical simulations of passive scalar mixing in turbulence. *Physica* D **239**, 1278–1287.

DONZIS, D. A., YEUNG, P. K. & SREENIVASAN, K. R. 2008 Dissipation and enstrophy in isotropic turbulence: scaling and resolution effects in direct numerical simulations. *Phys. Fluids* **20**, 045108.

ISHIHARA, T., GOTOH, T. & KANEDA, Y. 2009 Study of high-Reynolds number isotropic turbulence by direct numerical simulation. *Annu. Rev. Fluid Mech.* **41**, 165–180.

JEONG, J. & HUSSAIN, F. 1995 On the identification of a vortex. *J. Fluid Mech.* **285**, 69–94.

JIMENEZ, J., WRAY, A. A., SAFFMAN, P. G. & ROGALLO, R. S. 1993 The structure of intense vorticity in isotropic turbulence. *J. Fluid Mech.* **255**, 65–90.

KERR, R. M. 1985 Higher-order derivative correlations and the alignment of small-scale structures in isotropic numerical turbulence. *J. Fluid Mech.* **153**, 31–58.

NELKIN, M. 1999 Enstrophy and dissipation must have the same scaling exponents in the high Reynolds number limit of fluid turbulence. *Phys. Fluids* **11**, 2202–2204.

PUMIR, A. 1994 A numerical study of pressure fluctuations in three-dimensional, incompressible, homogeneous, tropic turbulence. *Phys. Fluids* **6**, 2071–2083.

SREENIVASAN, K. R. 1998 An update on the dissipation rate in homogeneous turbulence. *Phys. Fluids* **10**, 528–529.

SREENIVASAN, K. R. & ANTONIA, R. A. 1997 The phenomenology of small-scale turbulence. *Annu. Rev. Fluid Mech.* **29**, 435–472.

YAKHOT, V. 2008 Dissipation-scale fluctuations and mixing transition in turbulent flows. *J. Fluid Mech.* **606**, 325–337.

YAKHOT, V. & SREENIVASAN, K. R. 2005 Anomalous scaling of structure functions and dynamic constraints on turbulence simulations. *J. Stat. Phys.* **121**, 823–841.

YEUNG, P. K. & POPE, S. B. 1989 Lagrangian statistics from direct numerical simulations of isotropic turbulence. *J. Fluid Mech.* **207**, 531–586.